

An adaptive kernel regression method for 3D ultrasound reconstruction using speckle prior and parallel GPU implementation

Tiexiang Wen^{a,*}, Feng Yang^b, Jia Gu^a, Shifu Chen^{a,c}, Lei Wang^a, Yaoqin Xie^a

^a Shenzhen Institutes of Advanced Technology, Chinese Academy of Sciences, University Town of Shenzhen, 1068 Xueyuan Avenue, Shenzhen 518055, China

^b School of Biomedical Engineering, Southern Medical University, Guangzhou 510515, China

^c University of Chinese Academy of Sciences, No. 19(A) Yuquan Road, Shijingshan District, Beijing 100049, China

ARTICLE INFO

Article history:

Received 8 October 2016

Revised 16 March 2017

Accepted 5 June 2017

Available online 9 June 2017

Communicated by Dr Grana Manuel

Keywords:

Three-dimensional ultrasound imaging

Volume reconstruction

Kernel regression

Adaptive algorithm

GPU

ABSTRACT

Freehand three-dimensional (3D) ultrasound imaging is an attractive research area because it is capable of providing large field of view and high in-plane resolution image to allow better illustration of complex anatomy structures. However, reconstructed image is corrupted with speckle noise and artifacts in the conventional reconstructed volume data. In this paper, we propose a simple but effective adaptive kernel regression method for volume reconstruction from freehand swept B-scan images. By creating a linear model for estimating the homogeneous region of the B-scan image and learning the parameters of the model with a supervised learning method, the statistical characteristic of speckle can be well recovered. With the learned linear model of speckle, we can easily estimate the homogenous region and reconstruct image with speckle reduction and edge preservation via the adaptive turning of the smoothing parameters of the kernel regression. Our algorithm lends itself to parallel processing, and yields a 288× speedup on a graphics processing unit (GPU). Experiments on the simulated data, ultrasonic abdominal phantom and *in-vivo* liver of human subject and comparisons with some classical and recent algorithms are used to demonstrate its improvements in both volume reconstruction accuracy and efficiency.

© 2017 The Authors. Published by Elsevier B.V.

This is an open access article under the CC BY-NC-ND license.

(<http://creativecommons.org/licenses/by-nc-nd/4.0/>)

1. Introduction

During the past decades, two-dimensional (2D) ultrasound imaging has been recognized as the most often used imaging technique in clinical diagnosis and minimally invasive surgery [1]. Compared with the computer tomography (CT) and magnetic resonance imaging (MRI) modalities, ultrasound has won the popularity due to its low cost, portable, non-ionizing, and real-time imaging nature. However, conventional 2D ultrasound cannot provide 3D volume data for target localization and quantification, which is especially useful in assessing the progression of disease and guiding interventional and surgical procedures. In recent years, 3D ultrasound imaging has been developed to overcome such limitations by reconstructing volume data for allowing interactive visualization of the anatomical structures [2].

Several 3D ultrasound techniques have been reported in the literature in the past few years [3]. These techniques can be mainly grouped into two main categories: dedicated 3D probe and

3D imaging from a set of B-scan images acquired in a freehand scanning way. The former technique makes use of an array of piezoelectric elements in the probe, which is driven either by electronically steering the array elements or by an internal mechanical motor. The latter technique employs the conventional 2D ultrasound system and the spatial positioning system [4]. By integrating a positioning sensor into the conventional 2D ultrasound probe, successive B-scan images are acquired along with its corresponding position and orientation. Compared with the dedicated 3D probe, the latter freehand scanning method has its unique advantages, especially in the application of ultrasound-guided interventions, as it can provide inherent flexibility, large view of field and high in-plane resolution.

In freehand imaging, a spatial positioning sensor is attached to the ultrasound probe and provides the measurements of the position and orientation for each B-scan images. During freehand scanning, sequential B-scan images are collected along with its corresponding positioning information. The acquired B-scans are usually sparse and irregularly spaced as the freehand scanning way is highly subjective. There are mainly two approaches for freehand 3D ultrasound reconstruction: surface-based method and volume-based method. The first approach is based on surface reconstruc-

* Corresponding author.

E-mail address: tx.wen@siat.ac.cn (T. Wen).

tion of organs from image features (e.g., contours) detected in the acquired sequential ultrasound images [5]. In [6], a deformable surface model is proposed for surface estimation in cardiac ultrasound imaging. The second approach tries to reconstruct 3D regular volume grid from the stack of irregularly spaced B-scans via the interpolation or approximation algorithms. In comparison with the surface-based approach, the volume-based one can provide the whole volume data, which is especially useful for revealing the inner anatomical structure through the volume re-slicing tools and can be visualized either by volume rendering or by surface rendering technique.

A number of volume-based reconstruction methods for freehand 3D ultrasound imaging have been proposed in the literature [7]. Based on its implementation, the volume-based reconstruction method can be grouped into three categories [8]: voxel-based methods (VBM), pixel-based methods (PBM) and function-based methods (FBM). The VBM traverse all voxels in the target volume and insert corresponding pixels from the input B-scan images. As a classical means of VBM, voxel nearest neighbor (VNN) [9] interpolation method is widely used for its intuitive and straightforward implementation. VNN assigns each voxel value from the nearest pixel of the acquired B-scan images. VNN method could preserve the most original texture patterns from B-scan images. However, it could not suppress speckle noise and artifacts induced from the pixel intensity measurements. To provide a certain despeckling effect, the distance weighted (DW) algorithm is presented in [10], where each voxel value is computed by assigning the inverse-distance-weighted average of a set of pixels falling into a predefined 3D region centered at that voxel. The DW method performs well in reducing speckle and artifacts, but image edges are blurred as well because of the local average operation. To reconstruct image with speckle suppression and edge preservation, several modified DW methods have been reported based on the local statistics of pixels in the spherical region, including the adaptive distance-weighted (ADW) method [11–13] adaptive weighted median (AWM) filter method [14] and probe trajectory (PT) method [15]. Compared with the conventional DW method, those modified DW methods could provide improved results, but image blurring still could not be avoided. The PBM divide the volume reconstruction into two steps: bin-filling step (BFS) and hold-filling step (HFS). In BFS, each input pixel is traversed and its intensity value is assigned to one or several voxels. In HFS, the algorithm traverses on each voxel and fills any remaining empty voxels. The typical one is the pixel nearest neighbor (PNN) method [16], which runs through each pixel and assigns the pixel value into the nearest voxel. Averaging is performed for multiple contributions to the same voxel, but different variants of pixel distribution are possible, like the Bezier interpolation method [17], which makes use of the three-order Bezier curves defined by four control points locating at the same position of four adjacent B-scan images for approximating the voxels that intersecting each Bezier curve, and the Gaussian weighted reconstruction [18], which scatters pixels into the reconstructed volume based on the Gaussian kernel function. However, artifacts could be observed obviously on the boundaries between the highly detailed bin-filled region and the smoothed hole-filled region [7]. To reduce such artifacts, a fast marching method-based interpolation algorithm [19] is proposed by propagating the structural information along the normal direction of the evolving boundary. Speckle suppression is not addressed for the conventional PBMs. To reduce speckle, a Markov random field-based (MRF) filter [20] is introduced to despoke the PNN-reconstructed volume. In [21], a Bayesian-based nonlocal total variation method is introduced to reduce speckle noise for the acquired B-scan images before volume reconstruction. The FBM is another important means for volume-based reconstruction. It firstly builds the interpolation function from the input data and

then predicts voxel value of the target volume by evaluating function at regular interval. In [7], a radial basis function is introduced to estimate the underlying shape of the reconstructed volume data. In [22], an algorithm based on cyclic regularized Savitzky–Golay filters is introduced to deal with the scenario of mechanical linear scanning framework, which requires that all acquired B-scan slices are precisely parallel and evenly spaced. But such parallel scanning could not be easily satisfied for the freehand data acquisition. In [23], a classic kernel regression-based (CKR) interpolation method is proposed to make the improvement in terms of reconstruction accuracy. Generally, the FBM trends to suppress speckle noise but smooth out the image boundaries as well. And the performance of FBM is usually affected by the parameters of interpolation function.

3D ultrasound system attracts growing interest because it allows better illustration and precise volume analysis for complex anatomy structures. Volume reconstruction method plays an important role at providing the growing 3D ultrasound system with high quality image and fast reconstruction speed. Typical freehand 3D ultrasound system includes the IBIS NeuroNav system [24], which was a prototype neuronavigation system and used to acquire the intraoperative ultrasound images. Those freehand swept B-scans were then reconstructed into a 3D volume using a pixel-based method [8]. In [11], a portable freehand 3D ultrasound imaging system was developed for the assessment of musculoskeletal tissues. In [25], a sensorless 3D ultrasound imaging system was achieved based on speckle decorrelation tracking. Both of the imaging system of [11,25] utilized the ADW method to reconstruct the acquired B-scans into a 3D volume. In [26], a wireless 3D ultrasound system was developed for strain imaging, which is an important medical imaging tool for characterization of lesions. Since the mechanical translating device was used to precisely control the probe movement, relatively time-consuming interpolation algorithm has not be applied to the volume reconstruction in [26]. Meanwhile, to enhance the clinical practice of 3D ultrasound, the reconstruction algorithm has to be parallelized to achieve real-time or near real-time imaging. In [27], an incremental reconstruction method is designed to achieve near real-time freehand 3D ultrasound based on graphics processing unit (GPU). And the PNN method was used to perform hole-filling and failed to reconstruct volume with high image quality.

In this paper, we present a novel adaptive interpolation algorithm using local statistics of speckle for volume reconstruction of freehand ultrasound imaging. Unlike previous methods, a joint performance of image interpolation and speckle reduction is unified in the proposed kernel regression-based interpolation framework. The local statistics (i.e., variance and mean) is measured and used to create a linear model for the homogeneity estimation of the B-scan images. By learning the parameters of the linear model with a supervised learning method, the estimation between homogenous region and inhomogeneous region is built effectively. With the homogeneity estimation model, we can adaptively turn the smoothness behavior of the kernel regression function. If the variance calculated for the current voxel is below the homogeneity estimation of the linear model, the voxel is considered lying within a more homogenous region and large smoothness parameter is used to reduce speckle. Otherwise, small smoothness parameter is used to preserve image edges. The reconstruction accuracy is superior to that of prevailing volume reconstruction algorithms and the reconstruction speed is accelerated by the GPU-based parallel implementation, as we will show in Section 3.

The rest of the paper is organized as follows. The freehand 3D ultrasound system and the kernel regression-based interpolation method are described in Section 2.1 and Section 2.2, respectively. The local statistics of B-scan images are measured in Section 2.3. We present a novel homogeneity estimation model in Section 2.4.

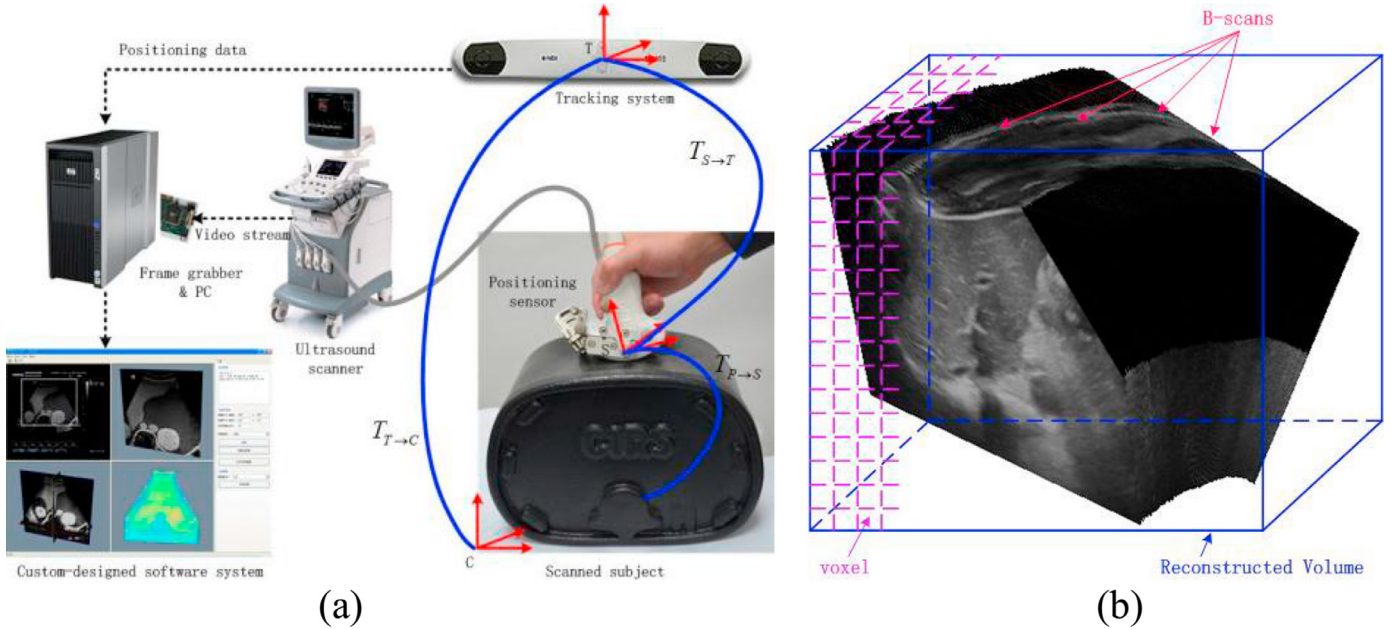


Fig. 1. Illustration of freehand 3D ultrasound system. (a) System configuration, (b) construction of 3D regular grid of voxels from the irregularly scanned B-scan images.

We will explain our new adaptive kernel regression-based interpolation method in Section 2.5. The GPU-based implementation of the adaptive kernel regression is described in Section 2.6. Experimental results are analyzed and presented in Section 3. Conclusion and discussion are drawn in Section 4.

2. Method

2.1. System description

In this study, a previously developed freehand 3D ultrasound scanning system [19] is used for data acquisition and volume visualization. The system was comprised of three parts, including a portable ultrasound scanner (DC-7, Mindray Medical International Ltd., Shenzhen, China), a spatial sensing device (Polaris, NDI, Ontario, Canada) and a workstation with custom-designed software system, which was programmed in VC++ and designed for data acquisition, volume reconstruction, visualization and data analysis. A positioning sensor of the spatial sensing device was attached to the probe of the ultrasound scanner (see Fig. 1(a)). The video stream $I = \{I_1, \dots, I_m\}$ containing m values of the ultrasound scanner was digitalized by a video capture card (RGB 133, VT Image Inc., Shenzhen, China) installed in the workstation. The position and orientation $T = \{T_1, \dots, T_m\}$ of the positioning sensor could be simultaneously recorded through RS232 serial port. An easy and reliable calibration procedure [28] is performed to ensure the accuracy of the position and orientation of the inspection plane.

In freehand scanning, the 2D probe is manipulated by sonographer in arbitrarily manner. As the probe is swept across the volume, sequential observed B-scan images are acquired along with its corresponding position and orientation of the scanning plane. Fig. 1(b) demonstrates a stack of typical acquired B-scan slices and its corresponding bounding box. The collection of irregularly spaced B-scan slices is then used to reconstruct a regular volume data.

2.2. Volume reconstruction based on kernel regression

The volume reconstruction problem for freehand 3D ultrasound imaging can be stated as follows: given a sequence of B-scan im-

ages $I = \{I_1, \dots, I_m\}$ with corresponding slice position and orientation $T = \{T_1, \dots, T_m\}$, the observed data can be constructed as $f(i) = (y_i, \mathbf{x}_i)$, where $y_i \in I$ is the gray intensity value measured by the ultrasound probe at the position $\mathbf{x}_i \in R^3$. For the construction of regular volume grid, we assume that the measurement model of ultrasound data is given by

$$y_i = r(\mathbf{x}_i) + \varepsilon_i \quad (1)$$

where $r(\cdot)$ is the regression function, ε_i is the independent and identically distributed noise. Assumed that $r(\cdot)$ is locally smooth to some order N , we can estimate the value of the regression function at a point \mathbf{x}_i via the generic local expansion about this point. Specifically, if \mathbf{x} is near the sample at \mathbf{x}_i , we have the following local Taylor expansion

$$\begin{aligned} r(\mathbf{x}_i) &= r(\mathbf{x}) + \nabla^T r(\mathbf{x})(\mathbf{x}_i - \mathbf{x}) + \frac{1}{2}(\mathbf{x}_i - \mathbf{x})^T \mathcal{H}(r(\mathbf{x}))(\mathbf{x}_i - \mathbf{x}) + \dots \\ &= \beta_0 + \boldsymbol{\beta}_1^T (\mathbf{x}_i - \mathbf{x}) + \boldsymbol{\beta}_2^T vech\{(\mathbf{x}_i - \mathbf{x})(\mathbf{x}_i - \mathbf{x})^T\} + \dots \end{aligned} \quad (2)$$

where ∇ and \mathcal{H} are the gradient (3×1) and Hessian (3×3) operators, respectively. $vech(\cdot)$ is the half-vectorization operator of the “low-triangular” portion of a symmetric matrix, i.e.,

$$vech\left(\begin{bmatrix} a & b & c \\ b & d & e \\ c & e & f \end{bmatrix}\right) = [a \ b \ c \ d \ e \ f]^T. \quad (3)$$

The scalar $\beta_0 = r(\mathbf{x})$ is the restored voxel value of interest and the vectors $\boldsymbol{\beta}_1$ and $\boldsymbol{\beta}_2$ are defined by

$$\boldsymbol{\beta}_1 = \nabla r(\mathbf{x}) = \left[\frac{\partial r(\mathbf{x})}{\partial \mathbf{x}_1}, \frac{\partial r(\mathbf{x})}{\partial \mathbf{x}_2}, \frac{\partial r(\mathbf{x})}{\partial \mathbf{x}_3} \right]^T \quad (4)$$

$$\boldsymbol{\beta}_2 = \frac{1}{2} \left[\frac{\partial^2 r(\mathbf{x})}{\partial \mathbf{x}_1^2}, 2 \frac{\partial^2 r(\mathbf{x})}{\partial \mathbf{x}_1 \partial \mathbf{x}_2}, 2 \frac{\partial^2 r(\mathbf{x})}{\partial \mathbf{x}_1 \partial \mathbf{x}_3}, \frac{\partial^2 r(\mathbf{x})}{\partial \mathbf{x}_2^2}, 2 \frac{\partial^2 r(\mathbf{x})}{\partial \mathbf{x}_2 \partial \mathbf{x}_3}, \frac{\partial^2 r(\mathbf{x})}{\partial \mathbf{x}_3^2} \right]^T \quad (5)$$

Utilizing least square formulation, $\boldsymbol{\beta}_n$ can be computed from the following optimization problem [29]

$$\min_{\{\beta_n\}} \sum_{i=1}^P [y_i - r(\mathbf{x}_i)]^2 \frac{1}{h} K\left(\frac{\mathbf{x}_i - \mathbf{x}^2}{h}\right) \quad (6)$$

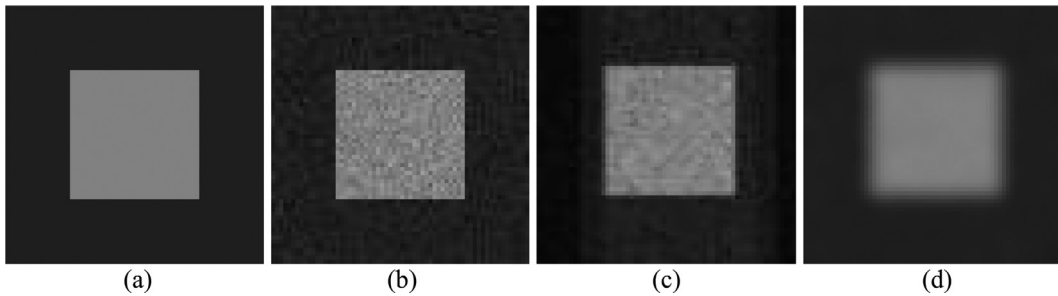


Fig. 2. Reconstruction results using different smoothing parameters for synthetic data. (a) Original image, (b) synthetic image with simulated speckle noise, (c) reconstructed image with $h = 0.5$, (d) reconstructed image with $h = 2.0$.

where P is the number of samples within the local neighborhood, $K(\cdot)$ is the kernel function which penalizes distance away from the local position where the approximation is centered, and h is the global smoothing parameter (i.e., bandwidth) that controls the strength of this penalty. The kernel function $K(\cdot)$ may be selected as a Gaussian, exponential, or other forms which satisfy the following constraints

$$\int tK(t)dt = 0, \int t^2K(t)dt = \text{const.} \quad (7)$$

It is known [30] that the kernel function has only a small effect on the accuracy of estimation. In this study, we prefer to select Gaussian kernel for its differentiability with low computational complexity. Eq. (6) can be expressed in a matrix form as a weighted least-squares optimization problem [31]

$$\mathbf{b} = \min_{\{\mathbf{b}\}} \|\mathbf{y} - \mathbf{X}_x \mathbf{b}\|_{\mathbf{W}_x}^2 = \min_{\{\mathbf{b}\}} (\mathbf{y} - \mathbf{X}_x \mathbf{b})^T \mathbf{W}_x (\mathbf{y} - \mathbf{X}_x \mathbf{b}) \quad (8)$$

where

$$\mathbf{y} = [y_1, y_2, \dots, y_p]^T \quad (9)$$

$$\mathbf{b} = [\beta_0, \beta_1^T, \dots, \beta_N^T]^T \quad (10)$$

$$\mathbf{W}_x = \text{diag}[K_h(\mathbf{x}_1 - \mathbf{x}), K_h(\mathbf{x}_2 - \mathbf{x}), \dots, K_h(\mathbf{x}_p - \mathbf{x})] \quad (11)$$

$$\mathbf{X}_x = \begin{bmatrix} 1 & (\mathbf{x}_1 - \mathbf{x})^T & \text{vech}^T \{ (\mathbf{x}_1 - \mathbf{x})(\mathbf{x}_1 - \mathbf{x})^T \} & \dots \\ 1 & (\mathbf{x}_2 - \mathbf{x})^T & \text{vech}^T \{ (\mathbf{x}_2 - \mathbf{x})(\mathbf{x}_2 - \mathbf{x})^T \} & \dots \\ \vdots & \vdots & \vdots & \dots \\ 1 & (\mathbf{x}_p - \mathbf{x})^T & \text{vech}^T \{ (\mathbf{x}_p - \mathbf{x})(\mathbf{x}_p - \mathbf{x})^T \} & \dots \end{bmatrix} \quad (12)$$

Since the primary goal of our volume reconstruction is to restore the voxel value of regular grid, the necessary computation is limited to estimate the parameter β_0 regardless of the estimator order N . Therefore, we can simplify the least-squares estimation as follows

$$\hat{r}(\mathbf{x}_i) = \beta_0 = \mathbf{e}_1^T (\mathbf{X}_x^T \mathbf{W}_x \mathbf{X}_x)^{-1} \mathbf{X}_x^T \mathbf{W}_x \mathbf{y} \quad (13)$$

where \mathbf{e}_1 is a column vector with first element equal to one and the rest equal to zero, $\hat{r}(\mathbf{x}_i)$ is the final voxel value estimated from its local samples.

Our previous work [23] has shown that the traditional kernel regression method has its superiority in terms of improving accuracy of reconstruction. However, the choice of the global smoothing parameter h affects the bias and variance of the estimate [32]. In general, smaller values for h result in sharper image (small bias and large variance) without noise removal. On the other hand, over-smoothing happens in regressions using large values for h , resulting in large bias and small variance. The reconstructed images with different smoothing parameters h are illustrated in Fig. 2, where the kernel regression is applied to the

synthetic cube data corrupted with Gamma distributed noise. It is clearly observed that the simulated speckle is still present in the reconstructed image for the small smoothing parameter $h = 0.5$. Otherwise, simulated speckle is reduced in the reconstructed image with blurred edges for the large smoothing parameter $h = 2.0$. Thus adaptive kernel regression method is urgently needed for the ultrasound volume reconstruction with the aim to reduce speckle and preserve edges. We will analyze the statistical property of speckle in the following section.

2.3. Speckle statistics

The presence of speckle generated by the interaction of acoustic wave with tissues leads to the low spatial resolution of ultrasound images. According to the recent study on speckle [33], it has found that Gamma probability density distribution is more suitable to describe the signal-dependent speckle noise for the Log-compressed ultrasound images. Generally, the acquired signal-dependent ultrasound data is modeled as

$$f = g + g^\gamma \cdot n \quad (14)$$

Where g is the noise-free data, n is the Gaussian noise with mean of zero and variation of σ_n^2 , γ is a factor that depends on ultrasound devices and additional processing related to image formation. This speckle model is flexible and capable of capturing reliable image statistics. Loupas et al. [34] have showed that $\gamma = 0.5$ model fits better than the Rayleigh model or the multiplicative model based on the experimental estimation of the mean versus the standard deviation for Log-compressed ultrasound images. In the remainder of the paper, $\gamma = 0.5$ is considered in the proposed algorithm.

Assuming that $g = \mu$ is constant in a homogenous region, we can observe from Eq. (14) that the variance σ^2 of the uniform region has the following linear relationship to the variance σ_n^2 of speckle noises

$$\sigma^2 = \mu \sigma_n^2. \quad (15)$$

For the homogenous region in ultrasound image, Eq. (15) shows that the variance is linearly proportional to the mean. The linear relation between the mean and variance of gray levels in B-scan images has been empirically verified in [35]. Eq. (15) implies that the ratio between variance and mean (i.e., σ^2/μ) can be used to characterize local image content. The linear model of Eq. (15) has been incorporated into a nonlocal means denoising algorithm for speckle filtering [36] and used by the ADW method for freehand ultrasound volume reconstruction [12].

The expected linear relationship between the local variance and the local mean can be used as a criterion to determine a homogenous region in the ultrasound image. In this study, the measurements of variance and mean are performed on conventional B-scan images captured from an ultrasound abdominal phantom

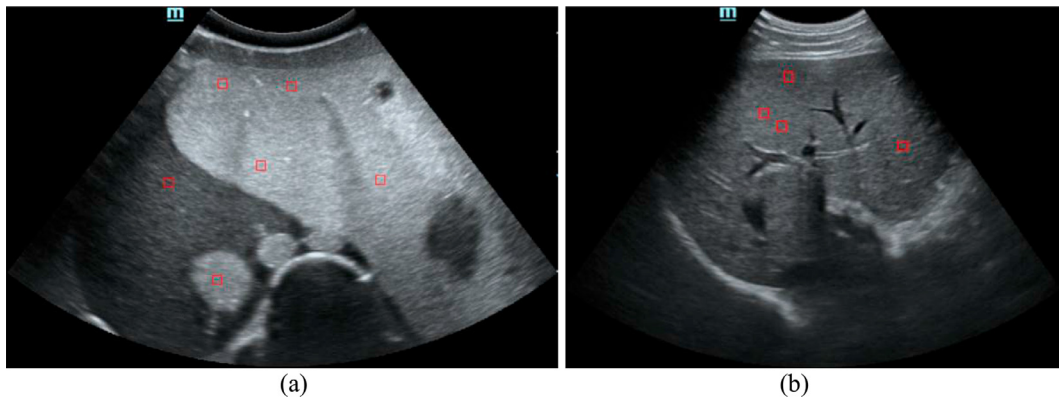


Fig. 3. Typical ultrasound images used for the measurements of local statistics in homogenous regions. (a) Measurement on the phantom B-scans, (b) measurement on the human liver B-scans.

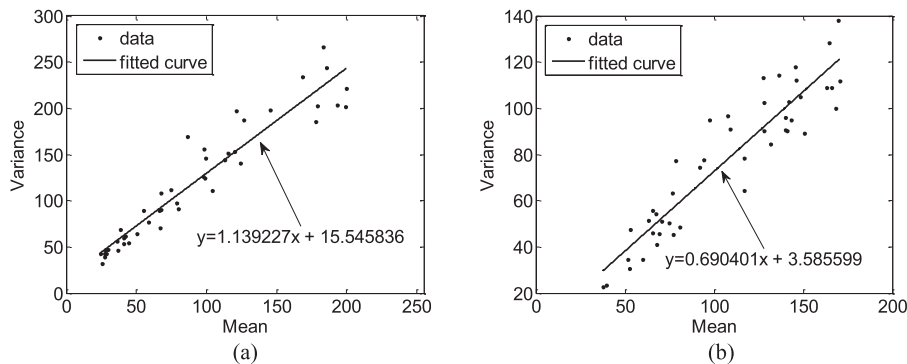


Fig. 4. Correlation between the local variance and mean for the homogenous region using linear fitting model. (a) The linear relationship for the phantom B-scans, (b) the linear relationship for the human liver B-scans.

Table 1
Pearson correlation coefficient between two variables variance and mean of homogenous region for the phantom and human liver B-scans.

Dataset	P	p-Value
Phantom B-scans	0.9539	4.2304e-024
Human liver B-scans	0.9263	7.6162e-020

[37] (Model 057, CIRS Inc., USA) and a healthy human subject's liver. The typical ultrasound image of the phantom and the human subject is given in Fig. 3(a) and Fig. 3(b), respectively. The local statistics including variance and mean are calculated within the homogenous regions, which are marked out with red rectangles in Fig. 3. For the measurement experiment, the window size of 15×15 pixels is chosen, which has been shown that it would be good at approximating speckle statistics in homogenous regions [12]. We use 45 measurements at different location for both the phantom and human liver B-scans with different B-scan imaging brightness. The measurement results are shown in Fig. 4, where the linear fitting model is used to build the correlation between the variance and the mean. Pearson correlation method is further used to verify the linear correlation between the variance and the mean for the measurement data. Table 1 indicates that there are strong linear correlation between these two variables both for the phantom and human liver B-scans (p -Value < 0.05). The asymptotic value of the σ^2/μ ratio is 1.14 and 0.69 for the phantom and human liver B-scans, respectively. To make the accurate expression about the linear relationship between the variance and the mean,

we will find the way to create a more robust parameter estimation model for the homogenous region in the following section.

2.4. Homogeneity estimation model

As the ratio between the variance and the mean can approximately represent the homogenous region of speckle, we use a more accurate linear model expressed as follows

$$\nu(N_k) = \alpha_0 + \alpha_1 m(N_k) + \varepsilon(N_k) \quad (16)$$

where N_k is the local homogeneous B-scan patch with size $|N_k| = (2d+1)^2$, $d \in \mathbb{N}$ centered at pixel k , $\nu(N_k)$ and $m(N_k)$ are the variance and the mean of local homogenous speckle patch, respectively, α_0 and α_1 are the unknown linear coefficients, $\varepsilon(N_k)$ is a random variable representing random error of the model. We assume a Gaussian density function for ε with zero mean and variance σ^2 (i.e., $\varepsilon(N_k) \sim N(0, \sigma^2)$). Based on the property of the Gaussian distribution, we have

$$\nu(N_k) \sim p(\nu(N_k)|N_k, \alpha_0, \alpha_1, \sigma^2) = N(\alpha_0 + \alpha_1 m(N_k), \sigma^2). \quad (17)$$

Then the joint conditional distribution can be written as

$$L = p(\nu(N_1), \dots, \nu(N_n)|N_1, \dots, N_n, \alpha_0, \alpha_1, \sigma^2) \quad (18)$$

where n is the total number of selected patches within the captured B-scan images, $\nu(N_n)$ is the variance of the n th homogenous patch, L is the likelihood. Assuming that the random error for each homogenous patch is independent and identically distributed, we

Algorithm 1 Homogeneity parameter estimation.

Input: the selected homogenous speckle patches $\{N_k\}$ from the B-scan images
Output: the linear coefficients α_0 and α_1 , the variable σ^2

Auxiliary functions:

- function for obtaining the size of the patches: $n = \text{size}(\{N_k\})$
- function for calculating the mean of the patches: $m(N_k) = \text{mean}(N_k)$
- function for calculating the variance of the patches: $v(N_k) = \text{variance}(N_k)$

Begin

- 1: $\alpha_0 = 0; \alpha_1 = 1;$
- 2: $sum = 0; wSum = 0; mSum = 0;$
- 3: **for** iteration from 1 to t
- 4: **for** index from 1 to n
- 5: $temp = v(N_k) - \alpha_0 - \alpha_1 m(N_k);$
- 6: $wSum = wSum + temp;$
- 7: $mSum = mSum + m(N_k) * temp;$
- 8: $sum = sum + temp^2;$
- 9: **end for**
- 10: $\sigma^2 = sum/n;$
- 11: $\alpha_0 = \alpha_0 + wSum / \sigma^2; \alpha_1 = \alpha_1 + mSum / \sigma^2;$
- 12: **end for**

End

can rewrite the likelihood Eq. (18) as

$$\begin{aligned} L &= \prod_{k=1}^n p(v(N_k) | N_k, \alpha_0, \alpha_1, \sigma^2) \\ &= \prod_{k=1}^n \frac{1}{\sqrt{2\pi\sigma^2}} \exp \left\{ -\frac{(\hat{v}(N_k) - \alpha_0 - \alpha_1 m(N_k))^2}{2\sigma^2} \right\} \end{aligned} \quad (19)$$

where $\hat{v}(N_k)$ denotes the ground truth variance of the k th image patch. Since $\hat{v}(N_k)$ is unknown for each scanned subject, the likelihood is usually computed by substituting observed $v(N_k)$ for ground truth $\hat{v}(N_k)$. Then the problem is to find the optimal values of α_0 , α_1 and σ to maximize L . For convenience, instead of maximizing the likelihood directly, we maximize the natural logarithm of the likelihood $\ln L$. From Eq. (19), the log likelihood function can be written in the form

$$\begin{aligned} \arg \max_{\alpha_0, \alpha_1, \sigma^2} \ln L \\ = \sum_{k=1}^n \ln \left(\frac{1}{\sqrt{2\pi\sigma^2}} \exp \left\{ -\frac{(\hat{v}(N_k) - \alpha_0 - \alpha_1 m(N_k))^2}{2\sigma^2} \right\} \right) \end{aligned} \quad (20)$$

Maximizing Eq. (20) with respect to variable σ , we have the maximum likelihood estimate for the variance as

$$\sigma^2 = \frac{1}{n} \sum_{k=1}^n (v(N_k) - \alpha_0 - \alpha_1 m(N_k))^2. \quad (21)$$

To maximize Eq. (20) with respect to the linear coefficient α_0 and α_1 , the gradient descent algorithm is used to estimate their values and can be expressed as

$$\alpha_j := \alpha_j + \frac{\partial \ln L}{\partial \alpha_j} \quad j \in \{0, 1\} \quad (22)$$

where the notation:= denotes the assignment of the value of α_j in the left term to be the value of the right term, $\partial \ln L / \partial \alpha_j$ is the partial derivative of $\ln L$ with respect to α_j and can be concisely written as

$$\frac{\partial \ln L}{\partial \alpha_0} = \frac{1}{\sigma^2} \sum_{k=1}^n (v(N_k) - \alpha_0 - \alpha_1 m(N_k)), \quad (23)$$

$$\frac{\partial \ln L}{\partial \alpha_1} = \frac{1}{\sigma^2} \sum_{k=1}^n m(N_k)(v(N_k) - \alpha_0 - \alpha_1 m(N_k)). \quad (24)$$

The procedure for estimating the linear coefficients α_0 , α_1 and the variable σ^2 is shown in Algorithm 1.

For each scanned subject, we use 45 selected homogenous patches to estimate the parameter of the linear model. The learning results are $\alpha_0 = 15.55$, $\alpha_1 = 1.14$, $\sigma = 19.61$ for the phantom B-scans, and $\alpha_0 = 3.59$, $\alpha_1 = 0.69$, $\sigma = 11.37$ for the human liver B-scans, respectively. In this paper, the dynamic homogenous threshold value H_k is set to the maximum variation of variance (i.e., $H_k = \alpha_0 + \alpha_1 m(N_k) + \sigma$). Once the values of the coefficients have been computed, these parameters will be used for the kernel regression reconstruction based on the adaptive smoothing strategy as described in the following section. It is worth noting that the linear parameters (i.e., α_0 , α_1 , and σ) depend on the imaging medium, the properties of the transducer, and vary across different ultrasound scanner [12,34]. Therefore, we have to learn the linear speckle model for different ultrasound scanner, different transducer and different imaging subject.

2.5. Adaptive kernel regression for volume reconstruction

It is known from Section 2.3 that the variance σ^2 is linearly correlated with the mean μ for the homogenous speckle regions. In this study, the linear model of Eq. (16) is used as a criterion and the homogenous estimation value H_k is computed dynamically for determining that whether a voxel is located in a homogenous region or not. Based on the local statistics of homogenous speckle region, the Heaviside-like function is introduced to make the adaptive selection of smoothing parameter h for kernel regression as follows

$$h_k = \begin{cases} h_a, & \text{if } v(N_k) > H_k \\ h_b, & \text{if } v(N_k) \leq H_k \end{cases} \quad (25)$$

where h_k is the adaptive smoothing parameter at k th voxel location, H_k is the dynamic threshold value of local homogeneity measured from the B-scan images for different scanned subjects, h_a and h_b are parameters which are empirically set with respect to the linear relationship between the variance and the mean. In our experiments, h_a and h_b are set to 0.5 and 2.0, corresponding to edge region and homogenous speckle region, respectively.

The choice of kernel size in parallel with the smoothness parameter h affects the edge sharpness of reconstructed image. In general, large kernel size results in large transitional boundary region. On the other hand, small transitional edge region is obtained for kernel regression using small kernel sizes. Edge preservation requires small kernel size, but the local statistics of homogenous speckle region could not be well approximated when the kernel size is too small. To reach a balance between speckle suppression and edge preservation, the strategy of dynamic determination

Algorithm 2 kernel<<blocks, threads>>.

Input: the input array A , the feature array X_x , the width of the volume W , the height of the volume H , the depth of the volume D , the window size of the kernel K_s .
Output: the output array A_o .

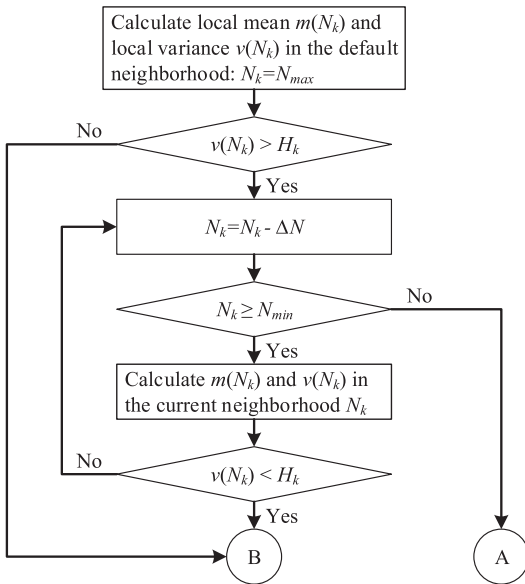
Auxiliary functions:

- function for obtaining the local data array centered at (i, j, k) with window size K_s :
 $out = Extract(in, i, j, k, K_s)$
- function for calculating the adaptive bandwidth: $h = Bandwidth(in)$
- function for calculating the dynamic weight array: $W_x = Weight(in)$

Do {

- 1: $x = threadIdx.x + blockDim.x * blockIdx.x;$
- 2: $y = threadIdx.y + blockIdx.y * blockDim.y;$
- 3: $offset = x + y * blockDim.x * gridDim.x;$
- 4: $k = offset / (W * H);$
- 5: $j = (offset - Z * (W * H)) / W;$
- 6: $i = offset - Y * W - Z * (W * H);$
- 7: $Y = Extract(A_i, i, j, k, K_s);$
- 8: $h = Bandwidth(Y);$
- 9: $W_x = Weight(h);$
- 10: $A_o(i, j, k) = \mathbf{e}_1^T (X_x^T W_x X_x)^{-1} X_x^T W_x Y;$
- 11: $offset += (blockDim.x * gridDim.x + blockDim.y * gridDim.y);$

While ($offset < W * H * D$)



A: The voxel is considered locating in an edge region.
B: The voxel is considered locating in a homogenous region.

Fig. 5. Flowchart for characterizing homogenous and edge regions with the dynamic kernel size method.

of kernel size is used to detect edge regions in this study. Fig. 5 shows this procedure for dynamically adjusting the kernel size of kernel regression. For the volume reconstruction of freehand 3D ultrasound imaging, the first step is to judge whether or not a voxel is locating in a homogenous region. The local variance $v(N_k)$ and the local mean $m(N_k)$ within the default maximum kernel size $N_k = N_{max}$ are calculated for the voxel. If the local variance $v(N_k)$ is no larger than the previously measured threshold value H_k , the voxel is considered locating in a uniform speckle region. Otherwise, a voxel's resolution ΔN is subtracted from the current kernel size N_k , i.e., $N_k = N_k - \Delta N$. Within the shrinkage kernel size, the local statistics are calculated again and used to determine whether or not the narrowed neighborhood is a homogenous speckle region not containing an object edge. This contraction of kernel size do not stop until the local variance $v(N_k)$ is below the homogeneity threshold H_k , or the kernel size reaches a pre-defined minimum

value N_{min} . For the latter case, the voxel is considered locating in a region containing edges.

2.6. Parallel implementation on graphics processors

Our algorithm is suited to parallel computation. In this paper, we realize the parallel implementation of the adaptive kernel regression using the programmable GPU. The NVIDIA Quadro M5000 processor used by us has 2048 32-bit processors organized as a single instruction multiple data (SIMD) stream processor. The GPU runs a kernel at a time. A kernel is a function that executes in parallel on the general-purpose programming model named CUDA (Compute Unified Device Architecture). In this model, the GPU device is viewed as co-processor to the host CPU. The kernel is organized in the form of “grid” that runs in parallel. The grid is composed of multiple “blocks” and each block can further be divided into multiple “threads”. Each thread can be distinguished and identified by a one-dimensional, two-dimensional or three dimensional index accessible within the kernel through the built-in *threadIdx*, *blockIdx*, *blockDim* and *gridDim* variables.

Based on the GPU implementation scheme, the pseudo code of the adaptive algorithm is given in Algorithm 2. The codes shown in lines 1–3 are used to obtain the linear voxel position from the kernel ID. In order to retrieve the value of 3D data array, the 1D linear index is converted into the 3D logical index of the data array in lines 4–6. Then the auxiliary function *Extract*, in line 7, is used to retrieve the nearby data array, which is centered at the position (i, j, k) with window size of K_s . The auxiliary function *Bandwidth*, in line 8, is used to dynamically adjust the kernel window size as illustrated in Fig. 5. And the auxiliary function *Weight*, in line 9, is used to compute the weight array according to the estimated bandwidth. Then the voxel value is estimated in line 10 according to Eq. (12). The main loop is repeated, in lines 11, to make sure that each voxel of the output array is accessed, even if the number of voxel exceeds the number of parallel threads.

3. Experimental results

To evaluate the performance of the proposed reconstruction algorithm, the simulated CT data and real ultrasound datasets acquired with our custom-designed freehand 3D ultrasound imaging system are experimented. The proposed adaptive kernel regression (AKR) algorithm is compared with the classic VNN algorithm [9], and some recent adaptive reconstruction algorithms aiming to suppress speckle such MRF [20], AWM [14], and ADW [12]. Moreover,

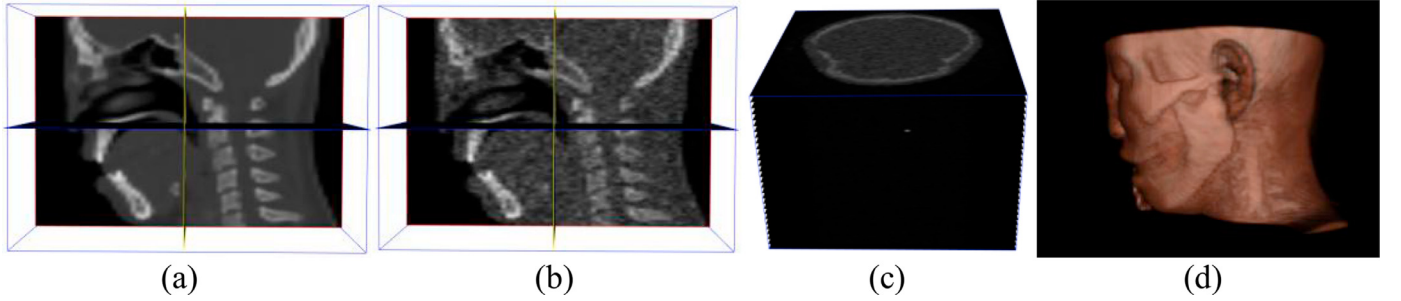


Fig. 6. CT volume data. (a) Original image, (b) image corrupted with Gamma noise, (c) scanned data with translational geometry, (d) volume rendering of the head dataset.

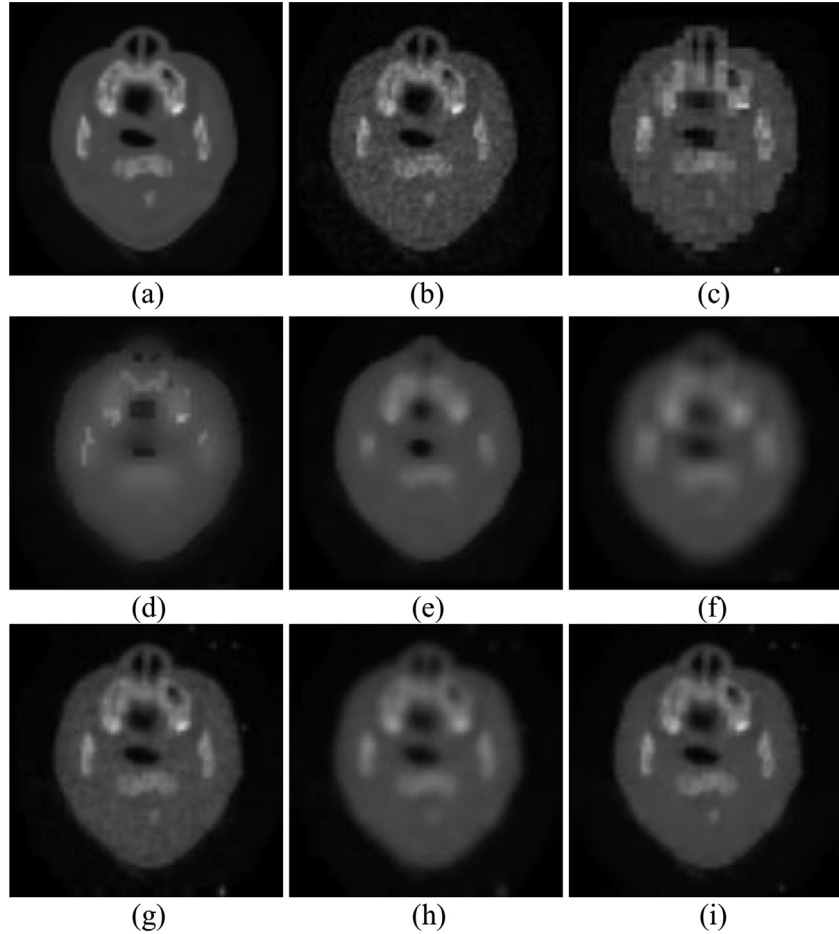


Fig. 7. Results along with the axial orientation obtained with different reconstruction methods for the simulated CT head data corrupted with Gamma noise. (a) Original image, (b) noise image, (c) VNN, (d) MRF, (e) AWM, (f) ADW, (g) CKR with $h = 0.5$, (h) CKR with $h = 2.0$, (i) AKR.

the classic kernel regression (CKR) [23] is also applied to the same dataset in order to evaluate the performance of our speckle-based AKR method. A leave-one-out method is used to evaluate the performance of the proposed algorithm for predicting the removed B-scan pixels. All the algorithms are implemented with the operating system of Windows 7 32-bit and the VC++ 2010, and the computer is equipped with Intel Core i5 2.6 GHz CPU with 4 processor cores and 8 GB RAM. A NVIDIA Quadro M5000 is used for GPU-accelerated volume reconstruction as described in [Algorithm 2](#).

3.1. Simulated experiment

Due to the lack of ground truth, it is a non-trivial task to make the accuracy evaluation of the methodology for volume reconstruction of freehand 3D ultrasound imaging. To be able to make the

comparable experiment with the predefined scanning geometry, we have developed a simulated acquisition of 2D B-scan images using the known test data that comprises a computerized tomography (CT) head dataset from the VTK database [38]. The speckle based on the Gamma noise distribution [Eq. \(14\)](#) with the mean of zero and the standard deviation of 1.3 is applied to the original CT volume to simulate the speckle noise in real ultrasound image. [Fig. 6\(a\)](#) and [\(b\)](#) depicts the original image and the observed image corrupted with Gamma noise. With the translational sweeps geometry, the CT volume dataset is re-sliced once every 3 slices, 4 slices and 5 slices, respectively. There are totally 48 slices, 36 slices and 29 slices, respectively, which are sampled and used for volume reconstruction. [Fig. 6\(c\)](#) and [\(d\)](#) gives an overall view for the translational sampled slices and the reconstructed volume visualized by ray-casting-based volume rendering.

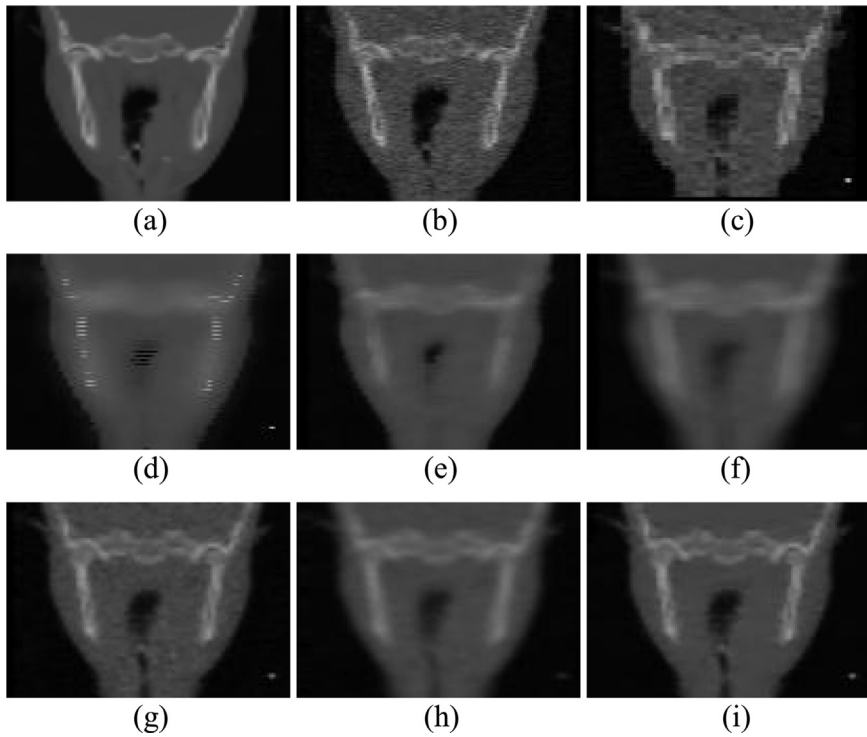


Fig. 8. Results along with the coronal orientation obtained with different reconstruction methods for the simulated CT head data corrupted with Gamma noise. (a) Original image, (b) noise image, reconstructed image with (c) VNN, (d) MRF, (e) AWM, (f) ADW, (g) CKR with $h = 0.5$, (h) CKR with $h = 2.0$, (i) AKR.

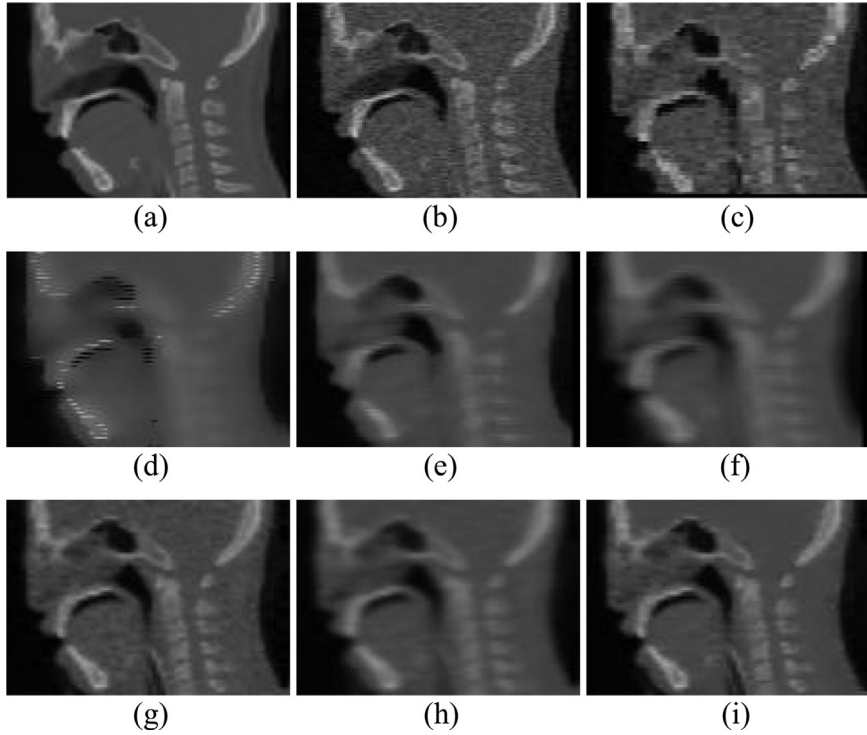


Fig. 9. Results along with the sagittal orientation obtained with different reconstruction methods for the simulated CT head data corrupted with Gamma noise. (a) Original image, (b) noise image, reconstructed image with (c) VNN, (d) MRF, (e) AWM, (f) ADW, (g) CKR with $h = 0.5$, (h) CKR with $h = 2.0$, (i) AKR.

For the qualitative comparisons among the VNN, MRF, AWM, ADW, CKR and AKR methods, Figs. 7–9 show the typical slices of the reconstructed image along the axial, coronal and sagittal orientation, respectively. For the visual comparison of edges and homogenous region, the intensity profiles along the center row of Figs. 7–9 images are illustrated in Figs. 10–12, respectively. As

shown in Figs. 7(c)–9(c) and Figs. 10(b)–12(b), the VNN method can preserve edges sharply, but it hardly removes the speckle noise in the homogenous region. The MRF, AWM and ADW methods work well at suppressing the speckle in the homogenous region, but they blur edges, which are not sharp any more as demonstrated in Figs. 10(c–e)–12 (c–e). The CKR's results are shown in

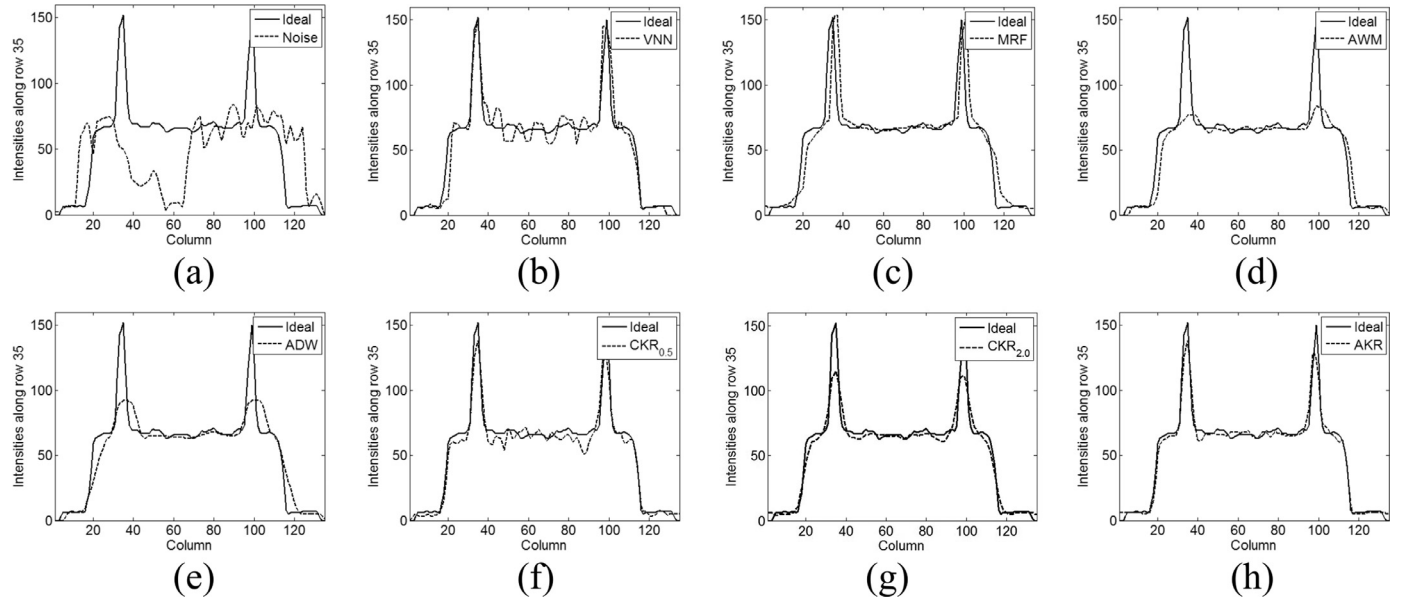


Fig. 10. The comparison of intensity profile along the center row of the axial slices in Fig. 7. (a) The ideal and observed, (b) the ideal and VNN, (c) the ideal and MRF, (d) the ideal and AWM, (e) the ideal and ADW, (f) the ideal and CKR with $h = 0.5$, (g) the ideal and CKR with $h = 2.0$, (h) the ideal and AKR.

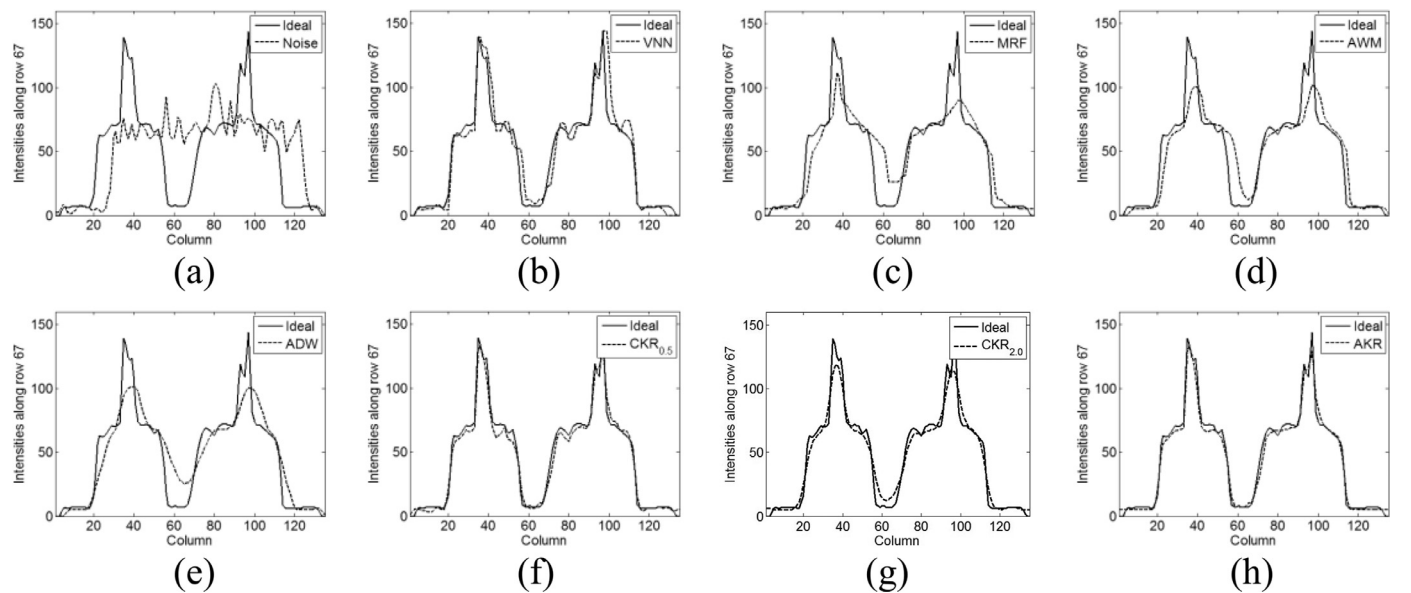


Fig. 11. The comparison of intensity profile along the center row of the coronal slices in Fig. 8. (a) The ideal and observed, (b) the ideal and VNN, (c) the ideal and MRF, (d) the ideal and AWM, (e) the ideal and ADW, (f) the ideal and CKR with $h = 0.5$, (g) the ideal and CKR with $h = 2.0$, (h) the ideal and AKR.

Figs. 7(g–h)–9(g–h) and Figs. 10(f–g)–12(f–g), which demonstrate that the performance of the CKR method is greatly affected by the bandwidth of the kernel function. If the bandwidth is small (e.g., $h = 0.5$), the reconstructed image has sharp edges but with the existence of speckle. Otherwise, the speckle can be removed but with the blurred edges (e.g., $h = 2.0$). As shown in Figs. 7(i)–9(i) and Figs. 10(h)–12(h), most of the speckle noise is removed in the homogenous region, and the edges and important features are well restored for the proposed AKR method. Visually, speckle reduction in homogenous speckle region and edge preservation in regions containing edges are adaptively achieved for the proposed AKR method.

For the quantitative comparisons, the averaged interpolation error (AIE) [7] and the mean structure similarity (MSSIM) [39] are used to compare objectively these methods. The AIE is defined and

calculated based on the following equation

$$\text{AIE} = \frac{1}{N} \sum_{i=1}^N |g(i) - f(i)| \quad (26)$$

where $g(\cdot)$ is the ground truth image, $f(\cdot)$ is the estimated image, and N is the number of pixels within the image $g(\cdot)$. A good reconstruction algorithm is capable of estimating the missing data with values close to the original data. Given $g(\cdot)$ and $f(\cdot)$, a low AIE value represents that the estimated result is satisfying while a high AIE means that the interpolation accuracy is poor.

The structure similarity (SSIM) image quality assessment index is a method for evaluating the ability to preserve the structural information of the algorithms. Based on the adaptation of intensity, contrast and structure, the SSIM index can be calculated by the

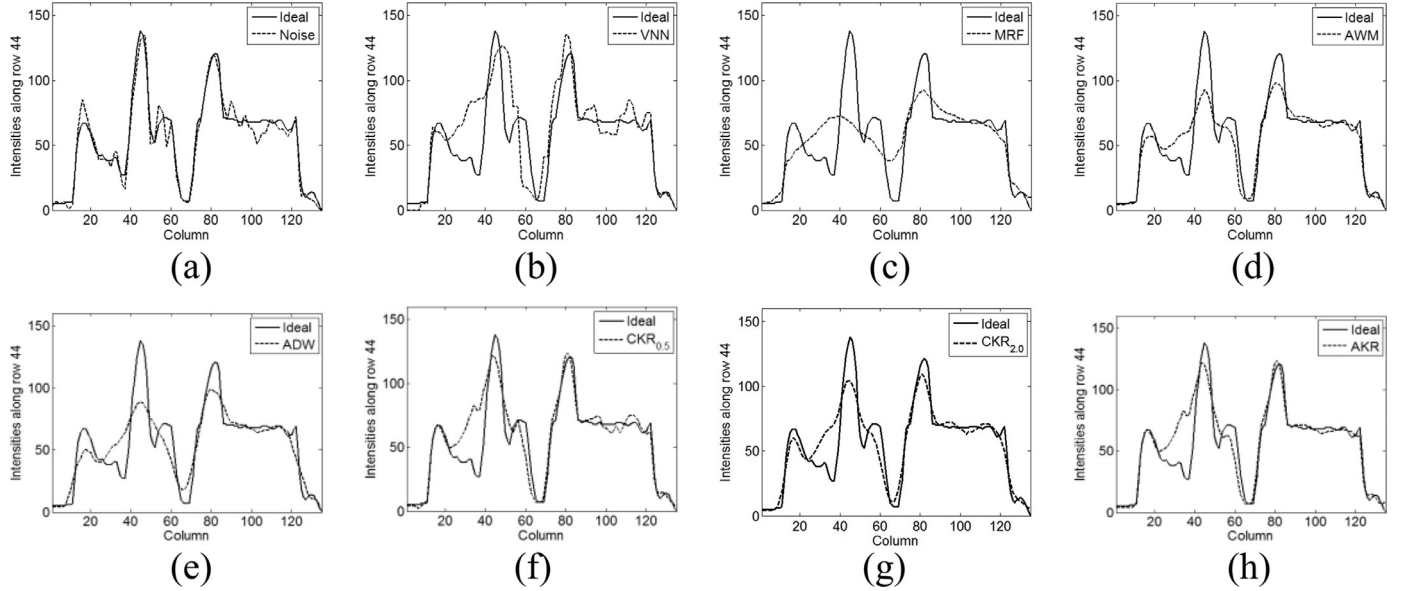


Fig. 12. The comparison of intensity profile along the center row of the sagittal slices in Fig. 9. (a) The ideal and observed, (b) the ideal and VNN, (c) the ideal and MRF, (d) the ideal and AWM, (e) the ideal and ADW, (f) the ideal and CKR with $h = 0.5$, (g) the ideal and CKR with $h = 2.0$, (h) the ideal and AKR.

Table 2
The AIE comparison for the simulated CT head data under different sampling rate.

Data sampling rate	VNN	MRF	AWM	ADW	CKR $_{h=0.5}$	CKR $_{h=2.0}$	AKR
Every 3 slice	6.34	5.98	4.46	5.41	4.06	4.50	3.92
Every 4 slice	6.93	6.60	5.91	5.89	4.12	4.57	4.03
Every 5 slice	7.05	6.89	6.38	6.37	4.20	4.58	4.18

Table 3
The MSSIM comparison for the simulated CT head data under different sampling rate.

Data sampling rate	VNN	MRF	AWM	ADW	CKR $_{h=0.5}$	CKR $_{h=2.0}$	AKR
Every 3 slice	0.8104	0.7351	0.7900	0.7776	0.9322	0.9009	0.9431
Every 4 slice	0.7905	0.7094	0.7683	0.7739	0.9066	0.8937	0.9212
Every 5 slice	0.7860	0.6963	0.7637	0.7706	0.8901	0.8847	0.9037

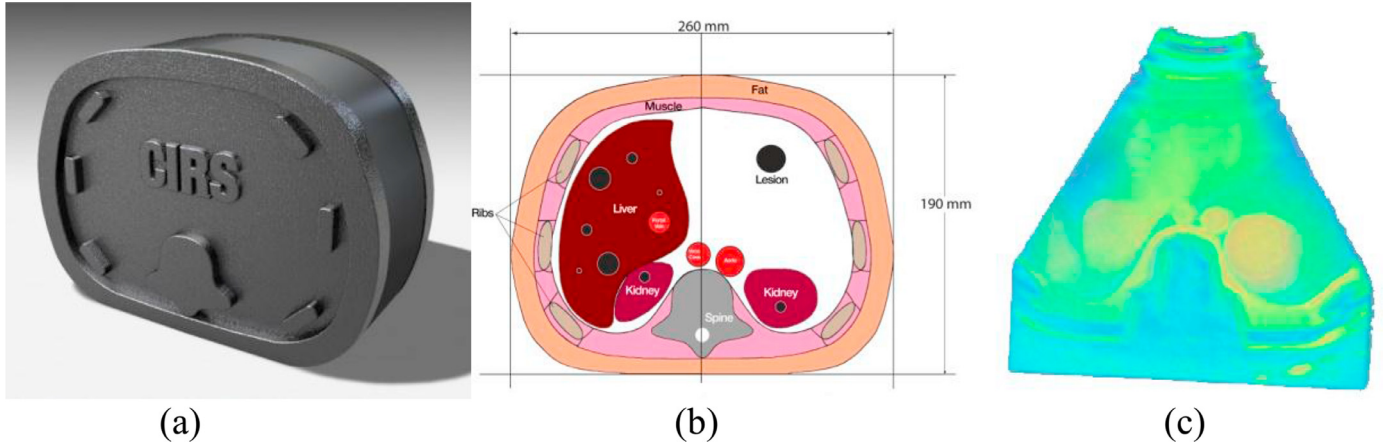


Fig. 13. The ultrasound abdominal phantom. (a) The outer structure of the phantom, (b) the inner structure of the phantom, (c) reconstructed volume.

following equation

$$\text{SSIM}(g, f) = \frac{(2\mu_g\mu_f + C_1)(2\sigma_{gf} + C_2)}{(\mu_g^2 + \mu_f^2 + C_1)(\sigma_g^2 + \sigma_f^2 + C_2)} \quad (27)$$

where μ_g , μ_f , σ_g , σ_f and σ_{gf} are the mean, variance and covariance of typical $8 \times 8 \times 8$ cube window, which moves voxel by voxel in images $g(\cdot)$ and $f(\cdot)$, respectively. The two constants $C_1 = k_1 L$ and $C_2 = k_2 L$ are used to stabilize the division with weak

denominator. Here, L is the dynamic range of voxel value (e.g., 255 for the 8-bit grayscale image), with $k_1 = 0.01$ and $k_2 = 0.03$ by default. Since the SSIM index is calculated on various windows of an image, the MSSIM is used in this experiment to assess the overall image quality

$$\text{MSSIM}(g, f) = \frac{1}{M} \sum_{i=1}^M \text{SSIM}(g(i), f(i)) \quad (28)$$

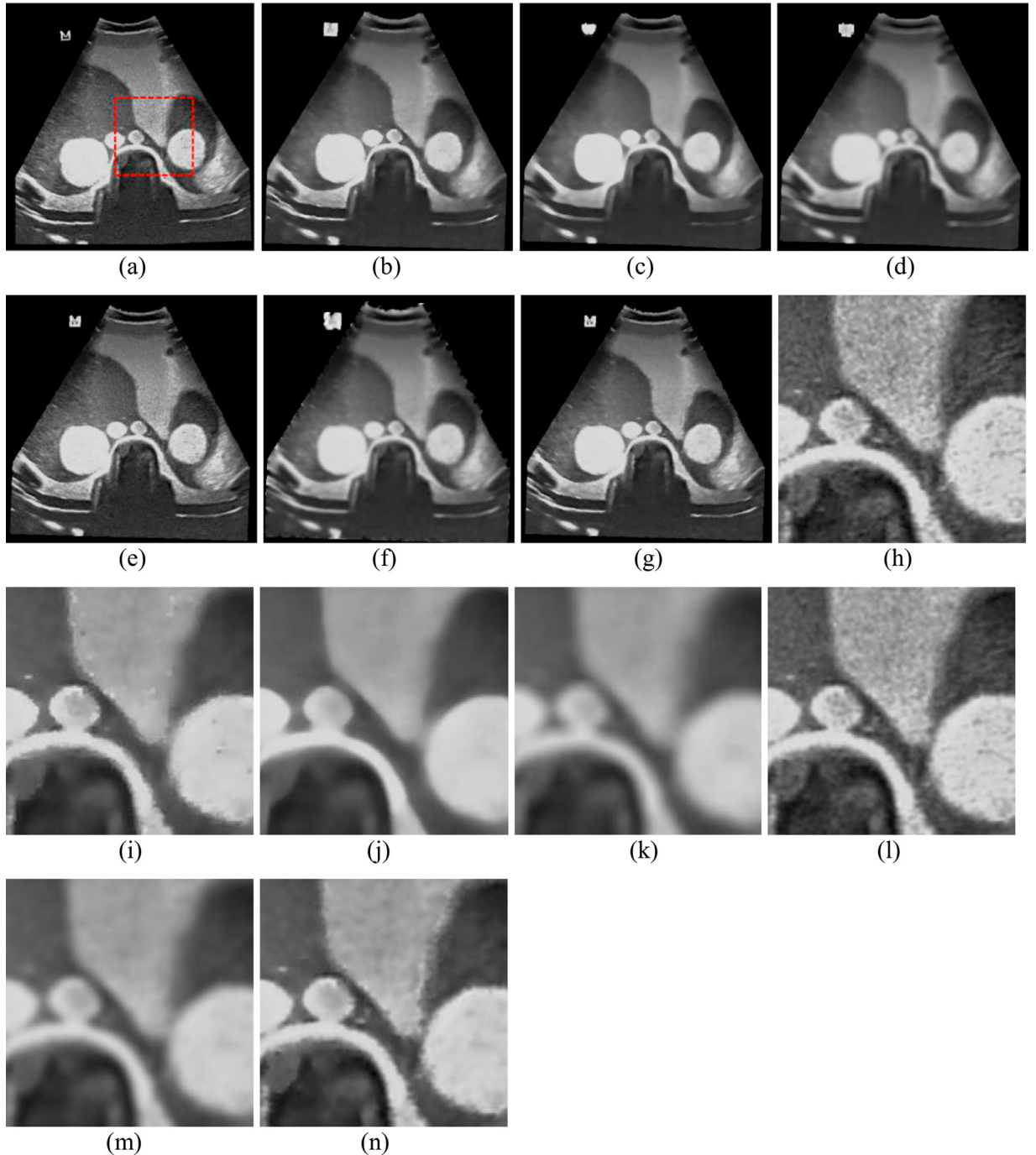


Fig. 14. Results along with the axial orientation obtained with different reconstruction methods for the phantom data. Reconstructed image with (a) VNN, (b) MRF, (c) AWM, (d) ADW, (e) CKR with $h = 0.5$, (f) CKR with $h = 2.0$ and (g) AKR. Images (h)–(n) are the magnified views of the selected regions in images (a)–(g).

where M is the number of local windows in the image. $\text{MSSIM}(g, f) \in [0, 1]$, and higher MSSIM value indicates better preservation of structural information between the ground truth image and the reconstructed image.

Since the original data is known for the simulated CT head data, the measurements of AIE and MSSIM for different algorithm can be computed directly between the ground truth volume and the reconstructed volume. Table 2 shows the AIE values obtained for each method. As can be seen, the results of VNN produce the highest AIE scores for all sampling rates. The high AIE value for VNN method indicates poor image quality because of the preservation of speckle texture pattern. For all levels of sampling

rate, the CKR method performs better than the MRF, AWM and ADW methods. In contrast, our AKR method achieves the lowest AIE in all cases. The AIE assessment index is affected higher by the speckle reduction in homogenous region than the edge preservation in regions containing structure information.

Table 3 shows the MSSIM of the results for the simulated CT head data. For this evaluation index, the results of VNN are higher than the results of MRF, AWM and ADW methods, indicating that much structural information in the images has been preserved. It is obvious that the MSSIM values of CKR are much higher than the other four methods except for the AKR method. And smaller bandwidth produces higher MSSIM scores for the CKR method, indicat-

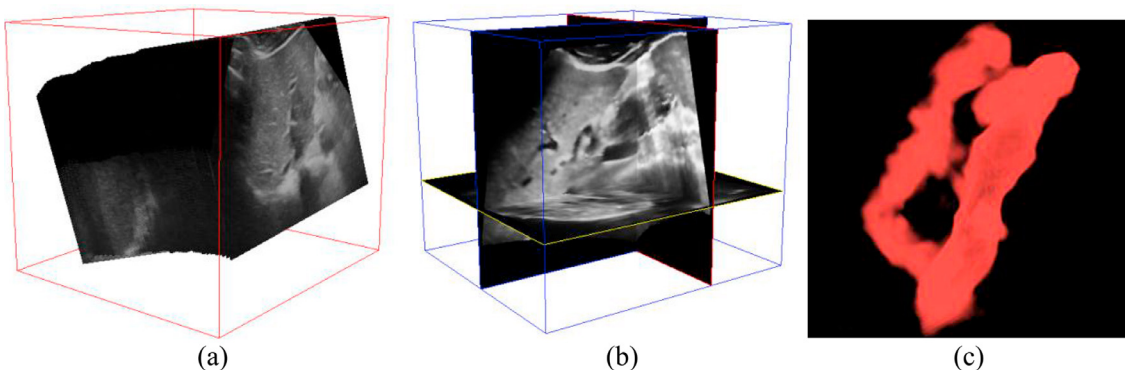


Fig. 15. The ultrasound human liver. (a) The acquired B-scans, (b) the reconstructed volume, (c) the segmented hepatic portal vein.

Table 4
The AIE comparison for the phantom data under different data removing ratio.

Data removing ratio (%)	VNN	MRF	AWM	ADW	CKR _{h=0.5}	CKR _{h=2.0}	AKR
100	7.40	9.89	8.87	8.61	7.39	9.62	7.37
300	9.24	11.17	10.71	11.39	8.74	9.82	8.44
500	10.18	10.50	10.42	10.81	9.28	10.02	9.06

Table 5
The AIE comparison for the liver data under different data removing ratio.

Data removing ratio (%)	VNN	MRF	AWM	ADW	CKR _{h=0.5}	CKR _{h=2.0}	AKR
100	6.02	7.75	7.62	6.80	5.98	7.45	5.42
300	8.42	9.73	9.88	9.44	8.19	9.12	8.15
500	10.49	10.88	11.50	11.46	9.79	9.80	9.63

Table 6
Averaged running time comparison (in seconds) of different algorithm for the ultrasound phantom and human liver data.

Data	VNN	MRF	AWM	ADW	CKR	AKR	AKR _{GPU}
Phantom (23,439,175 voxels = 425 × 421 × 131)	1027.22	1218.01	135.57	27.73	346.54	1125.23	3.90
Liver (45,782,100 voxels = 387 × 350 × 338)	3199.80	1971.20	203.55	38.69	667.56	2232.52	7.75

ing that edge preservation plays a more important role than the speckle reduction in homogenous region for the MSSIM assessment index. The AKR results achieve the highest MSSIM scores and lowest AIE scores, indicating that the proposed method outperforms the other five algorithms not only in speckle reduction but also in edge preservation.

3.2. Phantom ultrasound images

In this study, the experiment is conducted on an ultrasound abdominal phantom (Model 057, CIRS Inc., USA), which is made from proprietary materials to mimic various human tissues, including outer fat layer, liver with 6 lesions, kidneys with lesions, spine, partial lungs, portal vein, aorta and ribs. A 4.5 MHz abdominal probe is used to perform the freehand data acquisition. An interest region with size of 400 × 400 pixels is cropped for each B-scan slices. A depth setting of 200 mm is used resulting in a physical resolution of 0.50 mm/pixel. A totally 102 slices are acquired for the reconstruction of target volume with a dimension of 425 × 421 × 131. The picture of the phantom, its inner structure, and the reconstructed volume are illustrated in Fig. 13.

Fig. 14 shows a set of typical reconstructed results on real ultrasound abdominal phantom using the VNN, MRF, AWM, ADW, CKR and AKR methods, respectively. Visual inspection shows that

the VNN method overemphasizes the original texture patterns and preserves most of the speckle in the reconstructed image. The CKR with $h = 0.5$ method is good at speckle texture preservation as well as the VNN method. The MRF, AWM, ADW and CKR with $h = 2.0$ methods provide the significant speckle reduction, with the cost of excessive smoothing details. Visually, the proposed AKR method can suppress most of the speckles in the homogenous regions. Meanwhile, structural information is effectively preserved and sharpness is kept in the reconstructed image.

As the acquired B-scan images are corrupted by speckle noise and the ground truth is unknown for the real ultrasound images, the evaluation of the methodology for reconstruction of real ultrasound image is a non-trivial task. In our experiment, the leave-one-out method [7] is used to evaluate their ability of estimating the missing data. First, a B-scan slice n in the middle of the collection of the acquired B-scans is selected. All the pixels are then removed from the selected B-scan image. The rest of B-scan slices are used in the interpolation to fill the regular grid in the target volume. The deliberately removed pixels are recognized as the original data, which is used to make the comparison with the reconstructed data. Three different data removing ratios are used in the evaluation tests, i.e., 100%, 300% and 500%. For the 300% test, the pixels from B-scan n , B-scan $n - 1$ and B-scan $n + 1$ are totally

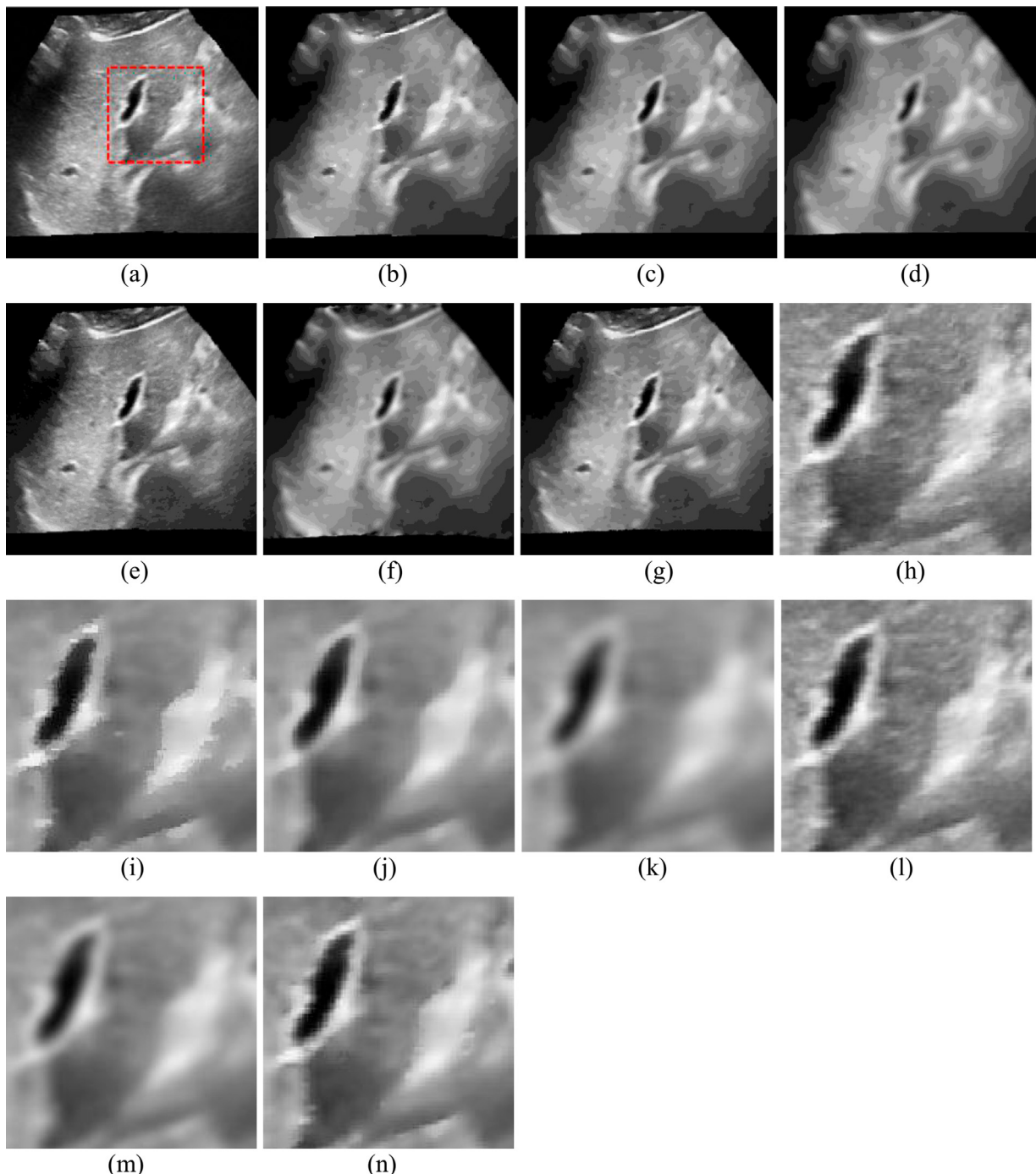


Fig. 16. Results along with the axial orientation obtained with different reconstruction methods for the liver data. Reconstructed image with (a) VNN, (b) MRF, (c) AWM, (d) ADW, (e) CKR with $h = 0.5$, (f) CKR with $h = 2.0$ and (g) AKR. Images (h)–(n) are the magnified views of the selected regions in images (a)–(g).

removed. The 500% test further remove B-scan $n - 2$ and B-scan $n + 2$. Table 4 shows the quantitative results of the AIE measurement for the phantom data. For the real ultrasound phantom data, the VNN method generates lower AIE values and performs better than the MRF, AWM and ADW methods. As opposed to the simulated CT volume data, the CKR method with large kernel size (i.e., $h = 2.0$) produces higher AIE values than the one with small kernel size (i.e., $h = 0.5$) and VNN method. The reason is that the deliberately removed data is corrupted with speckle noise and the VNN and CKR with $h = 0.5$ methods preserve most of the speckles in the reconstructed image. In comparison, the AKR method produces the lowest AIE score and offers competitive result compared to the other methods.

3.3. Liver ultrasound images

The third experiment is an examination of liver performed on a healthy human subject. Compared to previous studies, the clinical images contain more fruitful structure information, such as the liver, hepatic portal vein, gallbladder. A 4.5 MHz abdominal probe with a depth setting of 160 mm is used in the scanning sweep. A single sweep of the organ with a slow and steady motion resulted in a dense set of 167 B-scan slices just as shown in Fig. 15(a). Each B-scan image is cropped to 347×242 pixels giving a resolution of 0.46 mm/pixel. The final reconstructed volume with a dimension of $387 \times 350 \times 338$ and the exemplar hepatic portal venin are illustrated in Fig. 15(b) and (c).

Similar to the analysis of phantom data, Fig. 16 shows the exemplar reconstructed images of the human liver using the VNN, MRF, AWM, ADW, CKR and our AKR methods. For better comparisons, the same representative regions containing hepatic portal are selected and magnified for better visual comparison. And the leave-one-out approach is used to measure the AIE value in Table 5, where the quantitative performance is evaluated for different interpolation methods. From these results, we can obtain the conclusion similar to the ultrasound phantom data. The VNN and CKR with $h = 0.5$ methods overemphasize the speckle texture pattern. The MRF, AWM, ADW and CKR with $h = 2.0$ methods oversmooth many small resolvable objects as well as significant edges. Generally, the kernel regression based methods achieve better AIE values indicating the distinct improvement in reconstruction accuracy compared with previous methods. And the AKR method gives a better image contrast for the edges and speckle suppression compared to the CKR method.

3.4. Evaluation of computational efficiency

To evaluate the performance of computational efficiency of the proposed algorithm, the B-scan images are reconstructed into a volume data with the CPU-based methods (i.e., VNN, MRF, AWM, ADW, CKR and AKR) and the GPU-based AKR method (i.e., AKR_{GPU}). For efficiency comparison, Table 6 shows the average running time of different implementation of these algorithms on the ultrasound phantom and human liver data. For the CPU-based comparison, the CKR method runs slower than those PBMs (i.e., AWM and ADW) and faster than the VNN and MRF methods. We have given detailed analysis of the computational complexity for these methods in [23]. And the AKR method is relatively time-consuming and runs about 3.2 times slower than the CKR method due to the adaptive bandwidth calculation and dynamic kernel size determination. To enhance the clinical practice of the method, we accelerate the AKR method with the powerful GPU hardware. The results in Table 6 indicate that the processing time of the GPU-based AKR method can be accelerated up to 288 times over that of CPU for the phantom and liver, and the volume with size of 45 million voxels in our experiment can be reconstructed within 8 seconds. Hence, the computational efficiency of the proposed AKR method can be dramatically improved by the GPU acceleration.

4. Discussions and conclusion

In this paper, we have proposed an adaptive kernel regression method for freehand 3D ultrasound reconstruction. This algorithm was designed to suppress speckle in homogenous regions and preserve edges in inhomogeneous regions using local statistics prior. The Gamma distribution was employed to model the speckle for the acquired Log-compressed ultrasound image. We have created a novel linear model for the homogeneity estimation, based on the local correlation between variance and mean of the pixels within the B-scan image. With this simple but powerful prior and learning the parameters of the model using a supervised learning method, we achieved the adaptive tuning of the bandwidth parameter of the kernel regression. If a voxel was considered locating in a homogenous region, large bandwidth was used to smooth the uniform region. Otherwise, small bandwidth was selected to preserve edges. Furthermore, to alleviate the blurring effect for large kernel size, kernel size was dynamically adjusted in this study. Experiments were performed on the simulated CT volume, ultrasound phantom data and clinical human liver data by comparing six different reconstruction methods. The MSSIM and AIE quantitative metrics were used to evaluate the reconstruction accuracy of these interpolation methods. Experimental results

demonstrated that the proposed method yielded better performance in speckle suppression and edge preservation compared to those well accepted state-of-the-art interpolation algorithms. The quantitative result validated that our AKR method was a more accurate and robust reconstruction method for freehand 3D ultrasound imaging. Although the CPU-based serial implementation is relatively time-consuming, the GPU-based parallel implementation is satisfying and enhances the clinical practice of the AKR method.

Although we have found a way to model the homogeneity region with the local variance and local mean of the B-scan image, there are still some common problems to be solved. The first issue is that the resolution of an ultrasound image is known to vary spatially and directionally, i.e., the resolution is best near the focal spot, and the axial resolution is better than lateral resolution [8]. The second issue is that ultrasound is known to generate strong echoes when a reflective boundary is perpendicular to the beam, and weaker echoes from boundaries at larger angles [40]. In other words, the resolution and contrast in axial, lateral and elevational directions is not uniform. To overcome these challenges, some advanced models [40,41] can be taken into account. We leave these problems for our future research.

Acknowledgments

This study was financed partially by the National Natural Science Foundation of China (NSFC: 61401451, 61472411, 61271155, 61501444), the National High Technology Research and Development Program of China (2015AA043203), the Shenzhen Fundamental Research Project (JCYJ20150401145529039), the Shenzhen Engineering Laboratory for Key Technologies on Intervention Diagnosis and Treatment Integration and the Shenzhen Fundamental Research on the Intelligent Analysis of Digital Pathological Slice Imaging. The authors would like to thank the anonymous reviewers for their fruitful comments.

Reference

- [1] A. Fenster, J. Bax, H. Neshat, N. Kakani, C. Romagnoli, 3D ultrasound imaging in image-guided intervention, in: G. Gunarathne (Ed.), *Advancements and Breakthroughs in Ultrasound Imaging*, InTech, Rijeka, 2013, pp. 1–25.
- [2] E.D. Light, J.F. Angle, S.W. Smith, Real-time 3-D ultrasound guidance of interventional devices, *IEEE Trans. Ultrason. Ferroelectr. Freq. Control* 55 (9) (2008) 2066–2078.
- [3] R.W. Prager, U.Z. Ijaz, A.H. Gee, G.M. Treece, Three-dimensional ultrasound imaging, *Proc. Inst. Mech. Eng. H* 224 (2) (2010) 193–223.
- [4] S.J.E. Raul, M.F. Marcos, C.M. Pablo, A.L. Carlos, R.A. Juan, A theoretical framework to three-dimensional ultrasound reconstruction from irregularly sampled data, *Ultrasound Med. Biol.* 29 (2) (2005) 255–269.
- [5] G.M. Treece, R.W. Preager, A.H. Gee, L. Berman, Fast surface and volume estimation from non-parallel cross-sections, for freehand three-dimensional ultrasound, *Med. Image Anal.* 3 (2) (1999) 141–173.
- [6] H. Yu, M.S. Pattichis, C. Agurto, M.B. Goens, A 3D freehand ultrasound system for multi-view reconstructions from sparse 2D scanning planes, *Biomed. Eng. Online* 10 (2011) 7.
- [7] R.N. Rohling, A.H. Gee, L. Berman, A comparison of freehand three-dimensional ultrasound reconstruction techniques, *Med. Image Anal.* 3 (4) (1999) 339–359.
- [8] O.V. Solberg, F. Lindseth, H. Torp, R.E. Blake, T.A.N. Hernes, Freehand 3D ultrasound reconstruction algorithms – a review, *Ultrasound Med. Biol.* 33 (7) (2007) 991–1009.
- [9] S. Sherebin, A. Fenster, R.N. Rankin, D. Spence, Freehand three-dimensional ultrasound: implementation and applications, in: *Proceedings of Medical Imaging: Physics of Medical Imaging*, 1996, pp. 296–303.
- [10] C.D. Barry, C.P. Allott, N.W. John, P.M. Mellor, P.A. Arundel, D.S. Thomson, J.C. Waterton, Three-dimensional freehand ultrasound: image reconstruction and volume analysis, *Ultrasound Med. Biol.* 23 (8) (1997) 1209–1224.
- [11] Q.H. Huang, Y.P. Zheng, M.H. Lu, Z.R. Chi, Development of a portal 3D ultrasound imaging system for musculoskeletal tissues, *Ultrasonics* 44 (3) (2005) 153–163.
- [12] Q.H. Huang, M.H. Lu, Y.P. Zheng, Z.R. Chi, Speckle suppression and contrast enhancement in reconstruction of freehand 3-D ultrasound images using an adaptive distance-weighted method, *Appl. Acoust.* 70 (1) (2009) 21–30.
- [13] Q.H. Huang, Y.P. Zheng, A new adaptive interpolation algorithm for 3D ultrasound imaging with speckle reduction and edge preservation, *Comput. Med. Imaging Graph* 33 (2) (2009) 100–110.
- [14] Q.H. Huang, Y.P. Zheng, Volume reconstruction of freehand three-dimensional ultrasound using median filters, *Ultrasonics* 48 (3) (2008) 182–192.

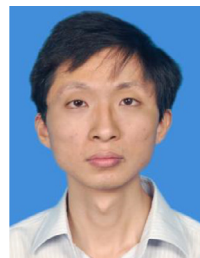
- [15] P. Coupe, P. Hellier, X. Morandi, C. Barillot, Probe trajectory interpolation for 3d reconstruction of freehand ultrasound, *Med. Image Anal.* 11 (6) (2007) 604–615.
- [16] T.R. Nelson, D.H. Pretorius, Interactive acquisition, analysis and visualization of sonographic volume data, *Int. J. Imaging Syst. Technol.* 8 (1) (1997) 26–37.
- [17] Q.H. Huang, Y.P. Zhang, W. Hu, X.L. Li, Bezier interpolation for 3-D freehand ultrasound, *IEEE Trans. Hum. Mach. Syst.* 45 (3) (2014) 385–392.
- [18] B. Kainz, M. Steinberger, W. Wein, M. Kuklisova-Murgasova, C. Malamateniou, K. Keradren, T. Torsney-Weir, M. Rutherford, P. Aljabar, J.V. Hajnal, D. Rueckert, Fast volume reconstruction from motion corrupted stacks of 2D slices, *IEEE Trans. Med. Imaging* 34 (9) (2015) 1901–1913.
- [19] T.X. Wen, Q.S. Zhu, W.J. Qin, L. Li, F. Yang, Y.Q. Xie, J. Gu, An accurate and effective FMM-based approach for freehand 3D ultrasound reconstruction, *Biomed. Signal Process. Control* 8 (6) (2013) 600–612.
- [20] J.M. Sanches, J.S. Marques, A Rayleigh reconstruction/interpolation algorithm for 3D ultrasound, *Pattern Recogn. Lett.* 21 (10) (2000) 917–926.
- [21] T.X. Wen, F. Yang, J. Gu, L. Wang, A novel Bayesian-based nonlocal reconstruction method for freehand 3D ultrasound imaging, *Neurocomputing* 168 (2015) 104–118.
- [22] P. Toonkum, N.C. Suwanwela, C. Chinrungrueng, Reconstruction of 3D ultrasound images based on cyclic regularized Savitzky–Golay filters, *Ultrasonics* 51 (2) (2011) 136–147.
- [23] X.K. Chen, T.X. Wen, X.M. Li, W.J. Qin, D.L. Lan, W.Z. Pan, J. Gu, Reconstruction of freehand 3D ultrasound based on kernel regression, *Biomed. Eng. Online* 13 (2014) 124.
- [24] L. Mercier, New prototype neuronavigation system based on preoperative imaging and intraoperative freehand ultrasound: system description and validation, *Int. J. Comput. Assist. Radio. Surg.* 6 (4) (2011) 507–522.
- [25] H.T. Gao, Q.H. Hunag, X.M. Xu, X.L. Li, Wireless and sensorless 3D ultrasound imaging, *Neurocomputing* 195 (2016) 159–171.
- [26] Z.H. Chen, Y.D. Chen, Q.H. Huang, Development of a wireless and near real-time 3D ultrasound strain imaging system, *IEEE Trans. Biomed. Circ. Syst.* 10 (2) (2016) 394–403.
- [27] Y. Dai, J. Tian, D. Dong, G. Yan, H. Zheng, Real-time visualized freehand 3D ultrasound reconstruction based on GPU, *IEEE Trans. Inf. Technol. Biomed.* 14 (6) (2010) 1338–1345.
- [28] P.W. Hsu, R.W. Prager, A.H. Gee, G.M. Treece, Rapid, easy and reliable calibration for freehand 3D ultrasound, *Ultrasound Med. Biol.* 32 (6) (2006) 823–835.
- [29] H. Takeda, S. Farsiu, P. Milanfar, Kernel regression for image processing and reconstruction, *IEEE Trans. Image Process* 16 (2) (2007) 349–366.
- [30] B.W. Silverman, *Density Estimation for Statistics and Data Analysis*, Chapman & Hall, New York, 1986.
- [31] N.K. Bose, N.A. Ahuja, Superresolution and noise filtering using moving least squares, *IEEE Trans. Image Process* 15 (8) (2006) 2239–2248.
- [32] D. Ruppert, M.P. Wand, Multivariate locally weighted least squares regression, *Ann. Stat.* 22 (3) (1994) 1346–1370.
- [33] P. Coupe, P. Hellier, C. Kervrann, C. Barillot, Nonlocal means-based speckle filtering for ultrasound images, *IEEE Trans. Image Process* 18 (10) (2009) 2221–2229.
- [34] T. Loupas, W. McDicken, P. Allan, An adaptive weighted median filter for speckle suppression in medical ultrasonic images, *IEEE Trans. Circ. Syst.* 36 (1) (1989) 129–135.
- [35] Z. Tao, H.D. Tagare, J.D. Beaty, Evaluation of four probability distribution models for speckle in clinical cardiac ultrasound images, *IEEE Trans. Med. Imaging* 25 (11) (2006) 1483–1491.
- [36] P. Coupe, P. Hellier, C. Kervrann, C. Barillot, Nonlocal means-based speckle filtering for ultrasound images, *IEEE Trans. Image Process* 18 (10) (2009) 2221–2229.
- [37] <http://www.cirsinc.com/products/all/65/triple-modality-3d-abdominal-phantom/>, 2013.
- [38] <http://www.vtk.org/download/>, 2016.
- [39] Z. Wang, A.C. Bovik, H.R. Sheikh, E.P. Simoncelli, Image quality assessment: from error visibility to structural similarity, *IEEE Trans. Image Process* 13 (4) (2004) 600–612.
- [40] C. Hennersperger, M. Baust, P. Waelkens, A. Karamalis, S.-A. Ahmadi, N. Navab, Multi-scale tubular structure detection in ultrasound imaging, *IEEE Trans. Med. Imaging* 34 (1) (2015) 13–26.
- [41] A. Karamalis, W. Wein, T. Klein, N. Navab, Ultrasound confidence maps using random walks, *Med. Image Anal.* 16 (6) (2012) 1101–1112.



Tiexiang Wen received the M.S. degree in biomedical engineering from Southern Medical University, China in 2008, and received the Ph.D. degree in computer science and technology from University of Chinese Academy of Sciences, China in 2014. He is currently an associate professor in Shenzhen Institutes of Advanced Technology, Chinese Academy of Sciences. His current research interests focus on medical imaging processing and image-guided interventions.



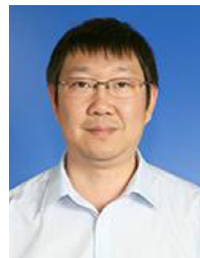
Feng Yang received the M.S. degree in biomedical signal and image processing from Sun Yat-Sen University, China in 1993, and received the Ph.D. degree in communication and electronic systems from South China University of Technology, China in 1998. He joined Division of Image Processing (LKEB) in Leiden University Medical Center, Netherlands, during April 2010 until April 2011 as a visiting scholar. His research interests include wavelet analysis, medical image processing and pattern recognition.



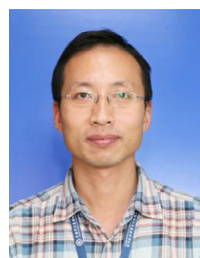
Jia Gu received his master and Ph.D. degree in 2001 and 2005 from Southeast University (China) and University of Rennes (France), respectively. He has working experiences in Samsung Advanced Institute of Technology (Beijing) and STI Medical Systems (Hawaii), on a wide variety of research projects on computer vision and medical imaging. Since 2008, he was recruited by Shenzhen Institute of Advanced technology of Chinese Academy of Sciences, as a full professor.



Shifu Chen is currently a Ph.D. candidate in Shenzhen Institutes of Advanced Technology, Chinese Academy of Sciences. He received M.S. degree in Computer Science from Institute of Computing, Chinese Academy of Science in 2010, and received the B.S. degree in Mathematics from Nanchang University in 2005. He worked as a senior system software engineer in NVIDIA from 2010 to 2014, and is a co-founder of HaploX Biotechnology. He is an open source software advocate and is the starter and owner of OpenGene projects for bioinformatics and next generation sequencing data analysis.



Lei Wang received the B.Eng. in Information and Control Engineering and Ph.D. in Biomedical Engineering, in 1995 and 2000, respectively. He was with University of Glasgow and Imperial College London, during 2001–2008. He is now with the Shenzhen Institutes of Advanced Technology, Chinese Academy of Sciences, as Professor and the Deputy Director with the Institute of Biomedical and Health Engineering. His research interests focus on Body Sensor Networks. He has published more than 200 scientific papers, authored nine books/book chapters, and filed 60 patents.



Yaoqin Xie received his B.Eng., M.Eng., and Ph.D. from Tsinghua University of China in 1995, 1998, and 2002, respectively. He was working in Peking University of China from 2002, and joined Shenzhen Institutes of Advanced Technology, Chinese Academy of Sciences, on 2010, as a Professor. He joined Stanford University as a postdoctoral fellow from 2006 to 2008. He has published more than 100 papers. He is a member of American Association of Physicist in Medicine (AAPM), a referee of Medical Image Analysis, Physics in Medicine and Biology, IEEE Transactions on Biomedical Engineering, IEEE Transactions on Information Technology in BioMedicine.